Mechanics of Materials 144 (2020) 103350

Contents lists available at ScienceDirect

Mechanics of Materials

journal homepage: www.elsevier.com/locate/mechmat

Research paper

An analytical model for shape morphing through combined bending and twisting in piezo composites

Jagannadh Boddapati[a], Shaswat Mohanty[1,b], Ratna Kumar Annabattula[*,b]

[a] Division of Engineering and Applied Science, California Institute of Technology, Pasadena, CA 91125, USA
[b] Department of Mechanical Engineering, Indian Institute of Technology Madras, Chennai 600036, India

ARTICLE INFO

Keywords:
Anisotropy
Bending and twisting
Bilayer
Electro-mechanical coupling
Piezo composite
Shape-morphing

ABSTRACT

Bilayer piezo macro fiber composites (MFCs) with specific fiber orientations are experimentally known to undergo bending as well as twisting, under the action of an externally applied electric field. An analytical model is developed for this shape-morphing phenomenon using continuum mechanics and energy minimization considering material anisotropy. A detailed parametric study is carried out using a coupled electro-mechanical finite element model and the results are used to validate the analytical model. The analytical model quantitatively predicts the variation of curvatures with the system parameters (bilayer geometry and electric field magnitude) with good accuracy. The tendency of a bilayer to undergo pure bending, pure twisting or a helical deformation is predicted using stress-free strain mismatch between anisotropic layers. Both bending and twisting deformations are found to be strongly dependent on the fiber orientation, vary linearly with the applied electric field magnitude, independent of length and decrease with an increase in width or thickness of MFC.

1. Introduction

Shape morphing structures that change shape upon application of external stimuli (Rosario, 2016; Oliver et al., 2016) have diverse applications ranging from NEMS (Cha and Daraio, 2018), micro-swimmers (Masoud et al., 2012; Nikolov et al., 2014), micro-grippers (Abdullah et al., 2018; Huang et al., 2016), drug delivery, biomedical applications (Randall et al., 2012) to morphing aircraft wings and windturbine blades (Martin and Gharib, 2018; Sofla et al., 2010; Lachenal et al., 2013) and many more (Chen et al., 2018). Actively controlling the stimulus is very important to use these structures effectively. Stimuli based on electric and magnetic fields offer faster actuation and shape changes compared to other stimuli like diffusion (Kim et al., 2018) and light (Zhao and Ikeda, 2009; White and Broer, 2015). Such structures are easily embeddable into electronics and are remotely controllable.

Piezo bimorphs are bilayer structures made of conventional thin piezoceramics. They are actuated with electric field and find good applications like x-ray mirrors (Signorato et al., 1998; Susini et al., 1995; Alcock et al., 2015) and energy harvesting (Oudich and Thiebaud, 2016). To increase the amount of actuation, at a given electric field, compared to these conventional bimorphs, macro fiber composites (MFCs) are developed by embedding piezo fibers into an epoxy matrix. These MFCs are typically bonded onto some thin inactive substrate and are used for actuating the substrates (Bent and Hagood, 1997). MFCs, due to their benefits of active shape morphing at low elastic stiffness, are finding increased usage in a wide range of applications like wing morphing (Williams et al., 2002; Paradies and Ciresa, 2009; Park and Kim, 2005) and are subjected to continued investigation even today.

While most of the existing piezo bilayers actuate and shape-morph only into pure bending structures, it is shown in the study carried out by Rosario (2016) that bilayer MFCs can also undergo twisting deformation in addition to bending, leading to the formation of structures that closely resemble helical structures. The generation of twisting is attributed to the material anisotropy created by the fiber layouts that are not coincident with principal geometric directions of the bilayer.

Even though several works in the literature that make use of anisotropy in generating combined large deformation twisting and bending, there are very few works that demonstrate this combined phenomena in piezoelectric samples. Kong and Wang (2003) have shown the formation of helical structures in Zinc Oxide (a piezoelectric

Abbreviations: MFC, Macro fiber composite; $P_{\theta_t-\theta_b}$, MFC with top layer orientation angle θ_t and bottom layer orientation angle θ_b; FEM, Finite element method; IDEs, Inter-digitated electrodes

* Corresponding author.
E-mail addresses: pboddapa@caltech.edu (J. Boddapati), shaswatm@stanford.edu (S. Mohanty), ratna@iitm.ac.in (R.K. Annabattula).
[1] Currently a graduate student in the Department of Mechanical Engineering, Stanford University, USA.

https://doi.org/10.1016/j.mechmat.2020.103350
Received 5 November 2019; Received in revised form 8 February 2020; Accepted 8 February 2020
Available online 10 February 2020
0167-6636/ © 2020 Elsevier Ltd. All rights reserved.

Nomenclature

L	length of the bilayer (m)
W	width of the bilayer (m)
H	thickness of the bilayer (m)
h	electric enthalpy density (J m^{-3})
$\boldsymbol{E}$	electric field vector (V m^{-1})
$\boldsymbol{E_t}$	top layer electric field vector (V m^{-1})
$\boldsymbol{E_b}$	bottom layer electric field vector (V m^{-1})
E_0	magnitude of electric field (V m^{-1})
$\tilde{\mathbf{E}}$	Green-Lagrangian deformation tensor (no units)
$\boldsymbol{C}$	elastic stiffness tensor (GPa)
$\boldsymbol{K}$	dielectric permitivity tensor (F m^{-1})
$\boldsymbol{e}$	piezoelectric stress tensor (C m^{-2})
$\boldsymbol{d}$	piezoelectric strain tensor (C N^{-1})
$\boldsymbol{d}_1$, $\boldsymbol{d}_2$, $\boldsymbol{d}_3$	directrix triad vectors
W	total electric enthalpy (J)
W_t	electric enthalpy of top layer (J)
W_b	electric enthalpy of bottom layer (J)
$\boldsymbol{D}$	dielectric displacement vector (C m^{-2})
$\boldsymbol{Q}$	transformation matrix (no units)
$\boldsymbol{F}$	deformation gradient tensor (no units)
$\boldsymbol{u}^*$	displacement vector field arising from a stress-free strain field (m)
$\boldsymbol{u_n}$	nodal displacement vector (m)
$\boldsymbol{X_n}$	undeformed nodal displacement vector (m)
$\boldsymbol{x}$	deformed bilayer shape (m)
$\boldsymbol{X}$	undeformed bilayer shape (m)
$\boldsymbol{f_n}$	deformed nodal displacement vector (m)
u_x^*	normal displacement arising from a stress-free strain field (m)
u_y^*	transverse displacement arising from a stress-free strain field (m)
$\boldsymbol{X}$	space vector (m)
X_1, X_2, X_3	space vector components along *x, y, z*-axes (m)
$\mathbf{e_1}$, $\mathbf{e_2}$, $\mathbf{e_3}$	global coordinate system
$\mathbf{ef_1}$, $\mathbf{ef_2}$, $\mathbf{ef_3}$	local coordinate system
C_{11}, C_{12}, C_{13}, C_{33}, C_{44}	constants of elastic stiffness tensor $\boldsymbol{C}$
e_{13}, e_{33}, e_{15}	constants of piezoelectric stress tensor $\boldsymbol{e}$
K_{13}, K_{33}	constants of dielectric permittivity tensor $\boldsymbol{K}$

Greek symbols

θ	fiber orientation angle (in degrees)
θ_t	top layer fiber orientation angle (in degrees)
θ_b	bottom layer fiber orientation angle (in degrees)
ϕ	electric potential (m^{-1})
κ	bending curvature (m^{-1})
τ	twisting curvature (m^{-1})
$\boldsymbol{\sigma}$	cauchy stress tensor (N m^{-2})
$\boldsymbol{\epsilon}$	elastic small strain tensor (no units)
$\boldsymbol{\epsilon}^*$	stress-free strain tensor (no units)
κ^*	dimensionless bending curvature (no units)
τ^*	dimensionless twisting curvature (no units)
β	correction function (no units)

material) at the nanoscale, proposed to be caused because of surface charges. The experimental work carried out by Rosario (2016) demonstrates twisting, but only at small deformation regimes. Therefore it is interesting to investigate the influencing factors on the large deformation of piezo bilayers. Since MFCs have low stiffness compared to the other existing piezoceramics, these materials are chosen for this study and the effects of other parameters in generating large deformation have been analyzed.

It is an established fact in the literature that some form of anisotropy is a strong guiding factor influencing shape-changing to helical configurations. Chen et al. (2011); Yu et al. (2017) demonstrate the formation of helical structures induced by material anisotropy under isotropic and anisotropic stretching in rubber sheets. Wu et al. (2013) demonstrate the formation of helical structures in light actuated hydrogels modulated with internal stresses. Spillmann et al. (2016); Wie et al. (2015) discuss electrically induced twisting in liquid crystal elastomers due to molecular tilt in liquid crystal. Liu et al. (2014); Huang et al. (2012) make use of bifurcations in obtaining twisted structures in rubber materials. Armon et al. (2011) study and describe nature-inspired elastically induced shape morphing. Here are few other articles that demonstrate twisting, engineered by microstructure orientation creating some form of anisotropy (Zhang et al., 2016; Huang et al., 2016; Jeon et al., 2017; Armon et al., 2011; Mao et al., 2016; Jeong et al., 2011; Kong and Wang, 2003; Vyas and Annabattula, 2018).

While most of the recent work focuses on demonstrating the anisotropy induced twisting experimentally, there are very few articles that analytically explain the shape morphing behavior by considering material anisotropy. While, Chen et al. (2011), Yu et al. (2017), and few others have explained the formation of helical structures analytically, the material system that they considered is isotropic, allowing for the use of classical Kirchoff rod theories. However, the piezoelectric materials are anisotropic, because of which the classical Kirchoff rod theory cannot be directly used. To develop an analytical model to study twisting mechanics, we adopt the ideas of Liu et al. (2014); Huang et al. (2012); Chen et al. (2011); Majidi et al. (2010); Yu et al. (2017) in calculating strain based on a pre-assumed deformed shape and obtain curvatures by minimizing the total energy. We extend their ideas and develop analytical model to anisotropic bilayer MFCs by embedding anisotropy into material's constitutive laws and capture trends due to the parameters involved and verify the model using numerical simulations. Most of the predictions regarding deformation are captured well by the analytical model, but it has its own limitations. Explanations are provided for the observed anomalies.

A significant progress in understanding the shape-morphing structures and the underlying mechanics has been the subject of interest in the past 5 to 7 years. With the advances in modern fabrication techniques, tailoring anisotropy locally is becoming relatively easier (Gladman et al., 2016; Kuang et al., 2019). Intricate microstructures are now realizable in achieving structures that shape morph into complicated shapes than simple helices (Boley et al., 2019; Kotikian et al., 2019). A culmination of all these makes understanding of the mechanics involved in the shape morphing relevant.

The rest of the paper is organized as follows. In Section 2 the general theory and the discussion on the twisting due to eigenstrain (stress-free strain) is presented. In Section 3 a detailed discussion on the analytical model and the key highlights of the formulation are presented. In Section 4 the numerical model setup, to validate the predictions for the curvatures postulated by the analytical formulation, is discussed. In Section 5 the results of the numerical study and their coherence with the analytical formulation are discussed.

2. Theory

2.1. Macro fiber composites

Macro fiber composites are fabricated by embedding unidirectional piezoelectric fibers in an epoxy matrix of low stiffness. The electric field is applied along the fibers' axial direction for maximum actuation. To apply the electric field along the fibers' axial direction, interdigitated

electrodes (IDEs) are used. Unlike conventional electrodes, these interdigitated electrodes lie in the same plane of fibers. The positive direction of the applied electric field corresponds to the direction of poling in the fibers. To maximize the area of contact between the IDEs and the piezoelectric fibers, a rectangular cross-section of piezoceramic composite is adopted (Bent and Hagood, 1997). The electric field produced by these electrodes can be taken to be nearly axial along the fibers (Nasser et al., 2008).

2.2. Model setup

The model architecture of bilayer macro fiber composite (MFC) that has been studied in this work is shown in Fig. 1. The red-colored space indicates the top layer, and the blue-colored space indicates the bottom layer. The white-colored region represents a thin interface layer. This thin interface layer is introduced for the sake of applying electrical boundary conditions in finite element simulations. A detailed discussion on this interface layer is given in Section 4, which discusses the numerical setup.

The global coordinate system $[\mathbf{e}_1, \mathbf{e}_2, \mathbf{e}_3]^{\mathrm{T}}$ is taken to be at the center of the fixed end of bilayer with $\mathbf{e}_1$, $\mathbf{e}_2$ and $\mathbf{e}_3$ aligned along the length, width and thickness directions, respectively. The angle that fibers (poling direction) make, measured counter-clockwise with the length direction, is taken as fiber orientation angle θ. The poling direction in the fibers is referred to as the fiber orientation angle. The fiber orientation angle for top and bottom layers are indicated by θ_{t} and θ_{b}, respectively. Since these composites are transversely isotropic, a local coordinate system is required to indicate transverse direction. A local coordinate system $[\mathbf{ef}_1, \mathbf{ef}_2, \mathbf{ef}_3]^{\mathrm{T}}$ is chosen such that $\mathbf{ef}_3$ is along the fiber orientation (poling direction) given by θ. $\mathbf{ef}_1$ is chosen along the thickness direction ($\mathbf{e}_3$) and $\mathbf{ef}_2$ is chosen such that it is orthogonal to the other axes $\mathbf{ef}_1$ and $\mathbf{ef}_3$ while maintaining right hand thumb rule. The global coordinate system, as well as a representative local coordinate system for the top layer, are shown in Fig. 1.

The electric field applied along the poling direction alone is considered. This electric field, aligned with the poling direction causes maximum elongation in the poling direction due to the piezoelectric phenomenon. The same magnitude of the electric field (E_0) is applied on top and bottom layers. From piezoelectricity theory, an electric field applied along the poling direction θ is equivalent to the electric field applied along the poling direction $\theta + 180°$, as both electric fields cause elongation of fibers in θ direction. The top and bottom MFC layers are taken to have the same length, width, and thickness. Length, and width of each layer of MFC are represented by '*L*', '*W*', while total bilayer thickness is represented by '*H*'. Thus, both layers are identical except for the fiber orientations (poling direction).

The influence of E_0, θ_{t}, θ_{b}, *L, W, H* on the deformation are studied in this work in a large deformation setting. Bilayer configuration made up with top layer fiber orientation θ_{t} and bottom layer fiber orientation θ_{b} is referred as $P_{\theta_{\mathrm{t}}-\theta_{\mathrm{b}}}$. The resulting deformation of the bilayer is characterized by bending curvature κ and twisting curvature τ.

2.3. Constitutive laws for transversely isotropic piezoelectric material

The electromechanical behavior of a piezoelectric material is described using the four variables stress $\boldsymbol{\sigma}$, strain $\boldsymbol{\epsilon}$, dielectric displacement vector $\boldsymbol{D}$ and electric field $\boldsymbol{E}$. The constitutive laws for linear piezoelectric materials are given by Eqs. (1) and (2), if strain $\boldsymbol{\epsilon}$ and electric field $\boldsymbol{E}$ are taken as independent variables (Majidi et al., 2010). These equations are written based on a suitable energy density, electric enthalpy (h) (Lines and Glass, 2001; Fang and Liu, 2013), given by Eq. (3), where repeated indices indicate Einstein summation rule.

$$\sigma_{ij} = C_{ijkl}\epsilon_{kl} - e_{kij}E_k \tag{1}$$

$$D_k = e_{kij}\epsilon_{ij} + K_{ki}E_i \tag{2}$$

$$h = \frac{1}{2}\sigma_{ij}\epsilon_{ij} - \frac{1}{2}D_iE_i = \frac{1}{2}C_{ijkl}\epsilon_{ij}\epsilon_{kl} - e_{ijk}E_i\epsilon_{jk} - \frac{1}{2}K_{ij}E_iE_j \tag{3}$$

Here, $\boldsymbol{C}$ refers to the fourth-order elastic stiffness tensor, $\boldsymbol{e}$ refers to the third-order piezoelectric stress tensor, and $\boldsymbol{K}$ refers to the second-order dielectric permittivity tensor.

The macro fiber composites made of transversely isotropic piezoelectric materials are also elastically transversely isotropic. There are five independent elastic constants, three independent piezoelectric stress coupling constants, and two dielectric permittivity constants (Lines and Glass, 2001; Fang and Liu, 2013; Hasanzadeh et al., 2019) for a transversely isotropic material. These constitutive relations (Eqs. (1) and (2)) are represented in component form using voigt notation in Eqs. (4) and (5) with these 10 material constants. These material constants for macro fiber composites are obtained from data sheets of a commercial MFC manufacturer's website (MFC, 2019) and are tabulated in Table 1.

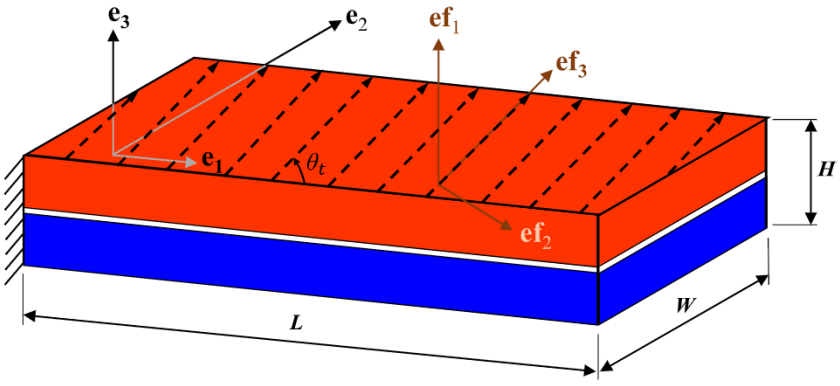

Fig. 1. Representative MFC bilayer setup (relative dimensions are not to scale).

Table 1
Material constants of macro fiber composites used in this study (MFC, 2019).

Constant	C_{11}	C_{12}	C_{13}	C_{33}	C_{44}	e_{13}	e_{33}	e_{15}	K_{11}	K_{33}
Value	19.45	7.34	8.19	35.36	5.51	−1.85	12.82	0	16.4	16.4
Units	GPa	GPa	GPa	GPa	GPa	$\frac{C}{m^2}$	$\frac{C}{m^2}$	$\frac{C}{m^2}$	$10^{-9}\frac{F}{m}$	$10^{-9}\frac{F}{m}$

$$\begin{bmatrix}\sigma_{11}\\ \sigma_{22}\\ \sigma_{33}\\ \sigma_{23}\\ \sigma_{31}\\ \sigma_{12}\end{bmatrix} = \begin{bmatrix} C_{11} & C_{12} & C_{13} & 0 & 0 & 0 \\ C_{12} & C_{11} & C_{13} & 0 & 0 & 0 \\ C_{13} & C_{12} & C_{33} & 0 & 0 & 0 \\ 0 & 0 & 0 & C_{44} & 0 & 0 \\ 0 & 0 & 0 & 0 & C_{44} & 0 \\ 0 & 0 & 0 & 0 & 0 & \frac{1}{2}(C_{11}-C_{12}) \end{bmatrix} \begin{bmatrix}\epsilon_{11}\\ \epsilon_{22}\\ \epsilon_{33}\\ 2\epsilon_{23}\\ 2\epsilon_{31}\\ 2\epsilon_{12}\end{bmatrix} - \begin{bmatrix} 0 & 0 & e_{31} \\ 0 & 0 & e_{31} \\ 0 & 0 & e_{33} \\ 0 & e_{15} & 0 \\ e_{15} & 0 & 0 \\ 0 & 0 & 0 \end{bmatrix} \begin{bmatrix}E_1\\ E_2\\ E_3\end{bmatrix} \tag{4}$$

$$\begin{bmatrix}D_1\\ D_2\\ D_3\end{bmatrix} = \begin{bmatrix} 0 & 0 & 0 & 0 & e_{15} & 0 \\ 0 & 0 & 0 & e_{15} & 0 & 0 \\ e_{31} & e_{31} & e_{33} & 0 & 0 & 0 \end{bmatrix} \begin{bmatrix}\epsilon_{11}\\ \epsilon_{22}\\ \epsilon_{33}\\ 2\epsilon_{23}\\ 2\epsilon_{31}\\ 2\epsilon_{12}\end{bmatrix} + \begin{bmatrix} K_{11} & 0 & 0 \\ 0 & K_{11} & 0 \\ 0 & 0 & K_{33} \end{bmatrix} \begin{bmatrix}E_1\\ E_2\\ E_3\end{bmatrix} \tag{5}$$

The components of tensors in constitutive laws used in Eqs. (4) and (5) are written in local coordinate system with $\mathbf{ef}_3$ direction aligned with the transverse isotropic direction/poling direction. Therefore, the tensor components are transformed into the global cartesian coordinate system for analysis. The transformation laws for second-order dielectric permittivity tensor $\boldsymbol{K'}$, third-order piezoelectric stress coupling tensor $\boldsymbol{e'}$, and fourth-order elastic stiffness tensor $\boldsymbol{C'}$ are given in the Eqs. (6), (7) and (8) respectively. The transformed tensor components are shown in Appendix A.

$$K'_{ij} = K_{ab}Q_{ia}Q_{jb} \tag{6}$$

$$e'_{ijk} = e_{abc}Q_{ia}Q_{jb}Q_{kc} \tag{7}$$

$$C'_{ijkl} = C_{abcd}Q_{ia}Q_{jb}Q_{kc}Q_{ld} \tag{8}$$

The transformation matrix used to transform tensor components from local to global coordinate system Sadd (2014a) in Eqs. (6) in (7) to (8) is given by Eq. (9).

$$\boldsymbol{Q} = \begin{bmatrix} 0 & \sin\theta & \cos\theta \\ 0 & -\cos\theta & \sin\theta \\ 1 & 0 & 0 \end{bmatrix} = \begin{bmatrix} \mathbf{e}_1.\,\mathbf{ef}_1 & \mathbf{e}_2.\,\mathbf{ef}_2 & \mathbf{e}_1.\,\mathbf{ef}_3 \\ \mathbf{e}_2.\,\mathbf{ef}_1 & \mathbf{e}_2.\,\mathbf{ef}_2 & \mathbf{e}_2.\,\mathbf{ef}_3 \\ \mathbf{e}_3.\,\mathbf{ef}_1 & \mathbf{e}_3.\,\mathbf{ef}_2 & \mathbf{e}_3.\,\mathbf{ef}_3 \end{bmatrix} \tag{9}$$

2.4. Mechanics of twisting deformation

It is important to understand the underlying mechanisms in guiding shape morphing as this would help in designing new complex structures with ease. Mechanics of twisting in these piezo composites can be easily comprehended by understanding how a single layer would behave in response to the electric field.

Consider an isolated single MFC layer, in which fiber orientation is at an arbitrary angle θ and is fixed at one end. If an electric field of magnitude E_0 is applied along the fiber orientation, it will cause the single layer to undergo stress-free deformation analogous to the thermal expansion of a steel rod when heated uniformly. This stress-free strain $\boldsymbol{\epsilon}^*$ is given by the Eqs. (10) and (12), where the tensor product $\boldsymbol{d} = \boldsymbol{C}^{-1}\boldsymbol{e}$ is called piezoelectric strain tensor. It has similar symmetries as $\boldsymbol{e}$.

$$\sigma_{ij} = C_{ijkl}\epsilon^*_{kl} - e_{kij}E_k = 0 \tag{10}$$

$$\epsilon^*_{kl} = C^{-1}_{ijkl}e_{pij}E_p \tag{11}$$

$$= d_{pkl}E_p \tag{12}$$

If components of $\boldsymbol{d}$ are represented in local coordinate system $\mathbf{ef}$, $\boldsymbol{\epsilon}^*$ attains the form shown in Eq. (13). From Table 1, since e_{15} is zero (so is d_{15}), shear strain in stress-free state is zero in local co-ordinate system. This shows that the basis vectors of the local coordinate system are the eigenvectors of $\boldsymbol{\epsilon}^*$ and as expected, the maximum principal strain is along the electric field direction $\mathbf{ef}_3$.

$$\epsilon^* = \begin{bmatrix} E_0d_{31} & 0 & 0 \\ 0 & E_0d_{31} & 0 \\ 0 & 0 & E_0d_{33} \end{bmatrix} \tag{13}$$

Upon transforming into global coordinate system, $\boldsymbol{\epsilon}^*$ attains the form shown in Eq. (14). Thus in global coordinates, the layer has both normal and shear strains.

$$\epsilon^* = \begin{bmatrix} E_0(d_{31}\sin^2(\theta) + d_{33}\cos^2(\theta)) & \frac{1}{2}E_0(d_{33}-d_{31})\sin(2\theta) & 0 \\ \frac{1}{2}E_0(d_{33}-d_{31})\sin(2\theta) & E_0(d_{31}\cos^2(\theta) + d_{33}\sin^2(\theta)) & 0 \\ 0 & 0 & E_0d_{31} \end{bmatrix} \tag{14}$$

For MFCs, $d_{31} \approx -0.1\ d_{33}$[2], $d_{15} = 0$. Thus, if the effect of d_{31} is neglected, the displacement field $\boldsymbol{u}^*$ of the free end of the MFC, obtained upon the integration of strain, is given by Eqs. (15a) and (15b).

$$u^*_x(X = L, Y) = (E_0d_{33}L)\cos^2(\theta) \tag{15a}$$

$$u^*_y(X = L, Y) = \left(\frac{1}{2}E_0d_{33}L\right)\sin(2\theta) \tag{15b}$$

In other words, neglecting d_{31} is equivalent to neglecting lateral displacements/deformations arising as a result of the Poisson effect. Displacement mismatch caused due to the Poisson effect would lead to secondary bending about width direction and this secondary bending is not observed in finite element simulations and hence neglected. In short, any displacement mismatch leading to the secondary bending

[2] Following a similar analogy for the relation between e_{33} and e_{31} as shown in Table 1.

about the width direction is neglected. This is summarized in Fig. 2 (for the case d_{31} neglected) with dashed black arrows representing fibers along θ direction, red color representing deformed shape, solid black arrow indicating the maximum extension along θ direction, u_x^*, u_y^* representing normal and transverse displacements, respectively.

From Eq. (15a), normal displacement u_x^* is maximum when fibers are oriented along the length direction ($\theta = 0°$) and minimum when fibers are oriented along the width direction ($\theta = 90°$). From Eq. (15a), transverse displacement u_y^* is maximum when fibers are oriented at $\theta = 45°$ and zero when fibers are oriented along the length or width directions ($\theta = 0° \ \& \ 90°$). These transverse displacements arise due to anisotropy and are absent in isotropic systems.

When two MFC layers with different fiber orientations are joined together, there is a mismatch between stress-free displacement fields $\boldsymbol{u}^*$ of both layers. This displacement mismatch guides the equilibrium shape of the bilayer. This is qualitatively depicted in Fig. 3 for different cases. If there is a mismatch only in normal displacement u_x^*, it leads to pure bending along the length direction (Fig. 3a). This effect is commonly observed in bending based shape morphing structures. If there is mismatch only in transverse displacement, u_y^* component, it leads to pure twisting with rotation about length direction (Fig. 3b). This scenario is possible if top and bottom layers have counter orientations ($\theta_t = \theta$, $\theta_b = -\theta$ or $-\theta + 180°$). The amount of twisting is directly proportional to the amount of mismatch. Thus twisting is maximum if $\theta_t = 45°$, $\theta_b = -45°$. Note that even in the pure twisting case, the normal displacement component is non-zero in both layers, but it is identical and hence no normal displacement mismatch and no bending is observed. If there is a mismatch in both normal and transverse displacements, it leads to the formation of helical structures (Fig. 3c).

Further, the equilibrium shape of any configuration with any arbitrary electric field can be predicted based on these arguments of a stress-free displacement mismatch. For example, if the electric field sign is reversed (opposite to poling) in one of the layers of a pure twisting sample, it will lead to the formation of helical structures as there will be a mismatch even in the normal displacement component. Thus an MFC bilayer can be actively transformed from a pure twisting configuration to a helical configuration just by reversing the sign of the electric field in one of the layers. This is an interesting advantage of using piezo active structures in terms of not only controlling the amount of displacement dynamically but also the mode of deformation.

3. Analytical model

3.1. Introduction

3.1.1. Assumptions for the analytical model

- We assume that an initially flat MFC bilayer shape-transforms into a helix with uniform bending and twisting (κ, τ). This assumption is valid as we observe from finite element simulations that the curvatures remain almost constant at a distance 10% away from both fixed and free edges.
- We assume that the bilayer is inextensible. Hence, stretching energy is neglected in energy formulation. This assumption is valid as we observe from finite element simulations that the stretch values are around 1.005.
- We assume that the MFC bilayer is undergoing large displacements, large rotations, but small strains. This assumption is valid as we observe from finite element simulations that the typical strain values go up to a maximum value of 0.01.
- We assume that the interface between two MFC layers is perfect and frictionless.
- We model macro fiber composite as a homogenized transversely isotropic linear elastic piezoelectric solid. We further assume that the material's constitutive law remains linear throughout its complete deformation range.
- We chose MFC's geometric parameters such that $L \geq 10W$, $W \geq 10H$. In this way, we can use beam theory results. We chose actual dimensions to be representative of MFCs available in the market.
- We neglect secondary bending effects along the width direction, arising out of displacement mismatch along the width direction. This assumption is valid as we don't observe any bending along the width direction in the finite element simulations.
- We assume that the centerline is the neutral axis for all the deformation scenarios.

3.1.2. Energy minimization

The main idea is to calculate the bilayer's total electric enthalpy (W) from electric enthalpy density given in Eq. (3). Total electric enthalpy energy (W) is obtained in Eq. (18) as the sum of electric enthalpy of both top and bottom layers. Since a helical configuration is a stable configuration for the bilayer, it's energy given by Eq. (18) should be a local minima with respect to the bending and the twisting curvatures κ, τ.

$$W_t = \int_{\Omega_t} \frac{1}{2}(\boldsymbol{\sigma}: \boldsymbol{\varepsilon} - \boldsymbol{D}.\boldsymbol{E})\mathrm{d}\Omega \tag{16}$$

$$W_b = \int_{\Omega_b} \frac{1}{2}(\boldsymbol{\sigma}: \boldsymbol{\varepsilon} - \boldsymbol{D}.\boldsymbol{E})\mathrm{d}\Omega \tag{17}$$

$$W = W_t + W_b \tag{18}$$

While stress $\boldsymbol{\sigma}$ and dielectric displacement vector $\boldsymbol{D}$, can be expressed in terms of strain $\boldsymbol{\epsilon}$ and electric field $\boldsymbol{E}$, the expression for strain ($\boldsymbol{\epsilon}$) is unknown. To find expressions for components of strain as a function of curvatures κ, and τ, the principles of differential geometry of helix are used as shown in the Section 3.2. Once the energy expression is obtained in terms of κ, τ, the following implicit Eqs. (19a) and (19b) are used to solve for curvatures. Due to the form of strain expression obtained in Eq. (29) as shown in the Section 3.2, strain($\boldsymbol{\epsilon}$) and hence stress ($\boldsymbol{\sigma}$) vary linearly with curvatures κ, τ. As a result the energy expression in Eq. (18) is quadratic in curvatures and hence Eqs. (19a) and (19b) result in implicit coupled linear equations which are then solved to obtain the curvatures.

$$\frac{\partial W}{\partial \kappa} = 0 \tag{19a}$$

$$\frac{\partial W}{\partial \tau} = 0 \tag{19b}$$

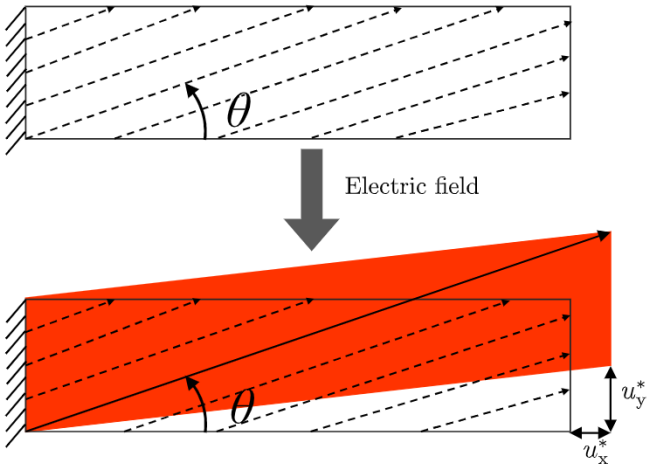

Fig. 2. Schematic denoting stress-free deformation in a single layer of MFC (deformation is not to scale).

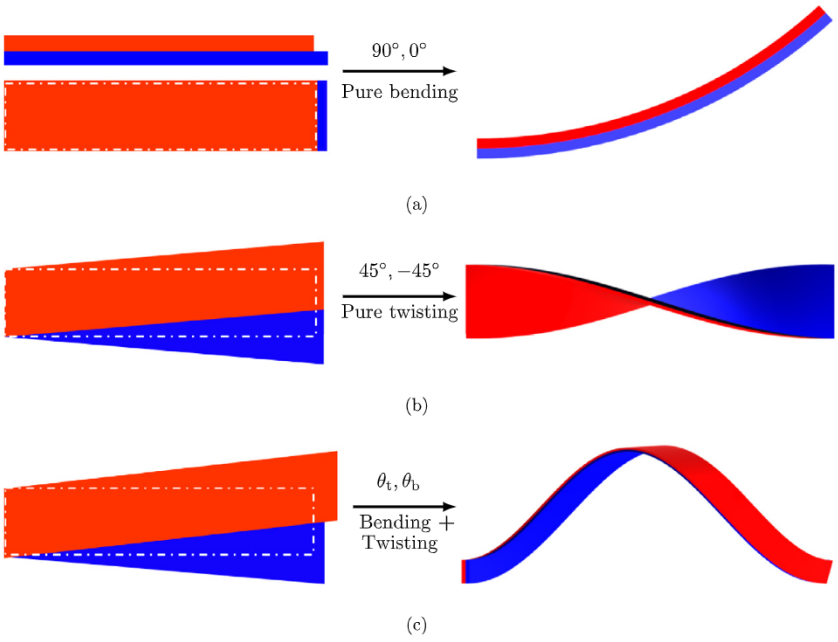

Fig. 3. Schematics showing different scenarios for (a) pure bending, (b) pure twisting and (c) combined bending and twisting (helical deformation) modes based on stress-free strain mismatch between two layers (deformation is not to scale).

3.2. Calculation of strain from differential geometry

Assume that the bilayer occupies the space of X_1, X_2, X_3, where $X_1 \in [0, L]$, $X_2 \in [-W/2, W/2]$ and $X_3 \in [-H/2, H/2]$, given by $\boldsymbol{X}$, as shown in Eq. (20). Upon application of electric field, the bilayer's shape transforms into a uniform helical configuration.

$$\boldsymbol{X}(X_1, X_2, X_3) = X_1\mathbf{e}_1 + X_2\mathbf{e}_2 + X_3\mathbf{e}_3 \tag{20}$$

The equation of center line of this helix configuration with bending and twisting curvatures (κ, τ) (Liu et al., 2014) could be described using Eq. (21), where $\gamma = \sqrt{\kappa^2 + \tau^2}$. Note that the slope calculated from Eq. (21) at the fixed end (s = 0) is non-zero.

$$\boldsymbol{y}(s) = \frac{\kappa}{\gamma^2}\sin(\gamma s)\mathbf{e}_1 + \frac{\kappa}{\gamma^2}(\cos(\gamma s) - 1)\mathbf{e}_2 + \frac{\tau}{\gamma}s\ \mathbf{e}_3 \tag{21}$$

The directrix basis for the helix $[\boldsymbol{d}_1, \boldsymbol{d}_2, \boldsymbol{d}_3]^{\mathrm{T}}$ can be calculated using Eqs. (22a)–(22c).

$$\boldsymbol{d}_1 \equiv \mathbf{y}' = \frac{\mathrm{d}\boldsymbol{y}}{\mathrm{d}s} = \frac{\kappa}{\gamma}\cos(\gamma s)\mathbf{e}_1 + \frac{\kappa}{\gamma}\sin(\gamma s)\mathbf{e}_2 + \frac{\tau}{\gamma}\mathbf{e}_3 \tag{22a}$$

$$\boldsymbol{d}_3 = \frac{\boldsymbol{d}_1'}{|\boldsymbol{d}_1'|} = -\sin(\gamma s)\mathbf{e}_1 + \cos(\gamma s)\mathbf{e}_2 \tag{22b}$$

$$\boldsymbol{d}_2 = \boldsymbol{d}_3 \times \boldsymbol{d}_1 = -\frac{\tau}{\gamma}\cos(\gamma s)\mathbf{e}_1 + \frac{\tau}{\gamma}\sin(\gamma s)\mathbf{e}_2 + \frac{\kappa}{\gamma}\mathbf{e}_3 \tag{22c}$$

Thus, the final configuration of all the points in the deformed configuration $\boldsymbol{x}(X_1, X_2, X_3)$ is described (by neglecting warping) using Eqs. (23) and (24). Here, by assuming that the rod has a negligible extension, X_1 is replaced by the parameter along the length in the deformed configuration denoted by s. s varies from 0 to L.

$$\boldsymbol{x}(s, X_2, X_3) = \boldsymbol{y}(s) + X_2\boldsymbol{d}_2 + X_3\boldsymbol{d}_3 \tag{23}$$

$$\begin{aligned} &= \left[\frac{\kappa}{\gamma^2}\sin(\gamma s) - X_2\frac{\tau}{\gamma}\cos(\gamma s) - X_3\sin(\gamma s)\right]\mathbf{e}_1 + \\ &\left[\frac{\kappa}{\gamma^2}(\cos(\gamma s) - 1) + X_2\frac{\tau}{\gamma}\sin(\gamma s) - X_3\cos(\gamma s)\right]\mathbf{e}_2 + \\ &\left[\frac{\tau}{\gamma}s + \frac{\kappa}{\gamma}X_2\right]\mathbf{e}_3 \end{aligned} \tag{24}$$

The deformation gradient $\boldsymbol{F}$ is given by Eq. (26).

$$\boldsymbol{F} = \frac{\partial \boldsymbol{x}}{\partial \boldsymbol{X}} = \begin{bmatrix} \frac{\partial x_1}{\partial X_1} & \frac{\partial x_1}{\partial X_2} & \frac{\partial x_1}{\partial X_3} \\ \frac{\partial x_2}{\partial X_1} & \frac{\partial x_2}{\partial X_2} & \frac{\partial x_2}{\partial X_3} \\ \frac{\partial x_3}{\partial X_1} & \frac{\partial x_3}{\partial X_2} & \frac{\partial x_3}{\partial X_3} \end{bmatrix} = \begin{bmatrix} \frac{\partial x_1}{\partial s} & \frac{\partial x_1}{\partial X_2} & \frac{\partial x_1}{\partial X_3} \\ \frac{\partial x_2}{\partial s} & \frac{\partial x_2}{\partial X_2} & \frac{\partial x_2}{\partial X_3} \\ \frac{\partial x_3}{\partial s} & \frac{\partial x_3}{\partial X_2} & \frac{\partial x_3}{\partial X_3} \end{bmatrix} \tag{25}$$

$$= \begin{bmatrix} \frac{\kappa}{\gamma}\cos(\gamma s) + X_2\tau\sin(\gamma s) - X_3\gamma\cos(\gamma s) & -\frac{\tau}{\gamma}\cos(\gamma s) & -\sin(\gamma s) \\ -\frac{\kappa}{\gamma}\sin(\gamma s) + X_2\tau\cos(\gamma s) + X_3\gamma\sin & \frac{\tau}{\gamma}\sin(\gamma s) & \cos(\gamma s) \\ (\gamma s) & & \\ \frac{\tau}{\gamma} & \frac{\kappa}{\gamma} & 0 \end{bmatrix} \tag{26}$$

The Green-Lagrangian strain tensor $\tilde{\boldsymbol{E}}$ is calculated from deformation gradient $\boldsymbol{F}$ using Eq. (28).

$$\boldsymbol{F}^T\boldsymbol{F} = \begin{bmatrix} (1 - \kappa X_3)^2 + \tau^2(X_2^2 + X_3^2) & \tau X_3 & -\tau X_2 \\ \tau X_3 & 1 & 0 \\ -\tau X_2 & 0 & 1 \end{bmatrix} \tag{27}$$

$$\tilde{\boldsymbol{E}} = \frac{1}{2}(\boldsymbol{F}^T\boldsymbol{F} - \boldsymbol{I}) = \frac{1}{2}\begin{bmatrix} -2\kappa X_3 + X_2^2\tau^2 + X_3^2\gamma^2 & \tau X_3 & -\tau X_2 \\ \tau X_3 & 0 & 0 \\ -\tau X_2 & 0 & 0 \end{bmatrix} \tag{28}$$

Note the shear strain and normal strain coupling in large deformation regime in Eq. (28). However, if, $\kappa \times H$ is less than 0.01, then the green-lagrangian tensor can be approximated as small strain tensor as shown in Eq. (29), by neglecting higher-order terms. From our FEM calculations, we find that $\kappa \approx 10\ \mathrm{m}^{-1}$, and $X_3 \approx 1\ \mathrm{mm}$ implies $\kappa X_3 \approx 0.01$. For these values, it is acceptable to neglect higher-order terms.

$$\tilde{\boldsymbol{E}} \approx \boldsymbol{\varepsilon} = \frac{1}{2}\begin{bmatrix} -2\kappa X_3 & \tau X_3 & -\tau X_2 \\ \tau X_3 & 0 & 0 \\ -\tau X_2 & 0 & 0 \end{bmatrix} \tag{29}$$

Eq. (29) represents the strain of a linear circular cross-section beam

under bending when torsion is absent together with the strain of a linear circular cross-section beam under torsion when bending is absent. Since the cross-section is non-circular, warping is to be considered while studying twisting. The exact warping function for an anisotropic thin beam in itself is not known and will not yield a simple closed-form expression if one wants to solve for them using the stress equilibrium equations. The closed-form expressions are much more complicated for the case of different layers having different orientations. Hence the warping function is not included in the strain calculation initially, in the transition from Eqs. (23) to (24). Instead, as an approximation, the result of torsion in thin elastic isotropic beams is used (Sadd, 2014b) in Eq. (30).

$$\epsilon \approx \frac{1}{2}\begin{bmatrix} -2\kappa X_3 & \tau X_3 & -(\beta)\tau X_2 \\ \tau X_3 & 0 & 0 \\ 0 & 0 & 0 \end{bmatrix} \tag{30}$$

According to Sadd (2014b), the strain component ϵ_{13} can be neglected for isotropic elastic thin rectangular shafts as an approximation. However, from finite element simulations, we did not observe coherent results by totally neglecting ϵ_{13} term in Eq. (29) as this would remove the dependence of strain on width. Instead of fully neglecting ϵ_{13} term, we prescribe a correction function (β) for ϵ_{13} in Eq. (30) whose value is very small (about 0.10, changes depending on the geometric parameters). The calculation of the exact warping function is bypassed by using this correction function. The correction function should be small if the H/W value is very small and approach zero as the bilayer gets thinner and wider as suggested by Sadd (2014b) (smaller H/W values). To obtain correction function, its values are adjusted for pure twisting configuration such that it matches FEM results. A curve fit is then created to find correction function for different aspect ratios that were not covered in finite element simulations. A linear fit is observed between correction factors adjusted using FEM and H/W as shown in Eq. (31) and in Fig. 4.

$$\beta = 1.286\frac{H}{W} + 0.024 \tag{31}$$

This correction function obtained for pure twisting configuration would not be same for other fiber orientations. However, finding the correction function for each possible fiber orientation pair (θ_t, θ_b) is not feasible. Using this correction function from pure twisting configuration to predict the curvatures for other configurations would introduce some error, but we found that this error is less than 10% (see Figs. 7 and 8). As seen in Fig. 4, the correction factor varies from 0.058 to 0.188 for high aspect ratio (W/H) of 40 to low aspect ratio (W/H) of 8.

The strain given by Eq. (30) is plugged into Eq. (18) for total energy of the bilayer and used to solve Eqs. (19a) and (19b). The tensor transformations, energy related integrations and differentiations are implemented in MATLAB using symbolic tools. The implicit linear equations Eqs. (19a) and (19b) are solved symbolically using MATLAB in-built function *solve*. The MATLAB code that prints analytical expressions for curvatures is provided in the supplementary information.

We note that the approximation for warping as well as the choice of the correction function are not rigorous. A detailed analysis involving the calculation of correction function would form the scope of further studies. We show that the approximate expression captures most of the trends qualitatively and quantitatively.

4. Finite element analysis

Finite element simulations are performed using commercial software ABAQUS (Simulia, 2012). The schematic for the MFC bilayer setup used for the numerical study is shown in Fig. 1. The general dimensions for the bilayer specimen are 200 mm × 10 mm × 0.5 mm ($L \times W \times H$).

The bilayer is fixed at one end, with all displacement degrees of freedom arrested as shown in Eq. (32). No external mechanical loading is applied. To obtain electric field along the desired fiber orientation/poling direction, a spatially varying electrical potential (ϕ) is prescribed as a boundary condition on the lateral faces of each layer, as shown in the Eqs. (33) and (34), such that its gradient produces electric field along the desired θ direction, as shown in the Eqs. (35) and (36), where E_0 denotes the magnitude of the desired electric field. With this way of applying electric potential, modeling complicated interdigitated electrodes is bypassed.

$$\boldsymbol{u} = [u_x\ u_y\ u_z]^T = [0\ 0\ 0]^T \quad \text{at} \quad x = 0 \text{ mm} \tag{32}$$

$$\phi_t = -E_0[x\cos(\theta_t) + y\sin(\theta_t)] \quad \forall\, z \in (0.01H,\ 0.5H) \tag{33}$$

$$\phi_b = -E_0[x\cos(\theta_t) + y\sin(\theta_t)] \quad \forall\, z \in (-0.5H,\ -0.01H) \tag{34}$$

$$\boldsymbol{E}_t = -\nabla\phi_t = E_0(\cos(\theta_t)\mathbf{e}_1 + \sin(\theta_t)\mathbf{e}_2) \tag{35}$$

$$\boldsymbol{E}_b = -\nabla\phi_b = E_0(\cos(\theta_b)\mathbf{e}_1 + \sin(\theta_b)\mathbf{e}_2) \tag{36}$$

Since the nodes shared by both layers cannot be specified with two distinct electric potentials simultaneously, a thin interface layer is introduced. The thickness of this interface layer is 2% of the total bilayer thickness, and no electric potential field is prescribed on the lateral boundary of the interface layer. Deformation was found to be insensitive to the interface layer thickness when it was varied from 2% to 5%.

Transversely isotropic material properties are assigned for top and bottom layers. Material constants used in the simulations are given in Table 1. The transverse direction is specified by creating local coordinate systems and assigning them to each layer separately. The interface layer is treated as an isotropic elastic material with Young's modulus of 20 GPa and Poisson's ratio of 0.3. The material constants for the interface layer are chosen such that its mechanical properties are close to MFC material properties.

To account for large displacements, the simulations have been carried out in the finite strain framework by switching on *Nlgeom* option in ABAQUS. Abaqus/Standard along with Newton-Raphson solver are used for solving the system of electromechanically coupled nonlinear equations. The top and the bottom layers are discretized using 20-noded quadratic brick, reduced integration piezoelectric elements (C3D20RE), while the interface layer is discretized using 20-noded quadratic brick reduced-order integration general-purpose continuum elements (C3D20E). The size of the mesh is kept the same along the length and the width direction such that the size of the element is 1 mm × 1 mm, with three such elements through the thickness of each layer. The interface layer is discretized with same element dimensions along the length and the width direction, but with just one element through the thickness. This results into the discretization of the entire domain into 7000–28,000 elements depending on the dimensions of the bilayer under study. The accuracy of the mesh is verified through detailed mesh refinement analysis, the results to which are presented in Appendix C. Quadratic C3D20RE elements were used to obtain a better

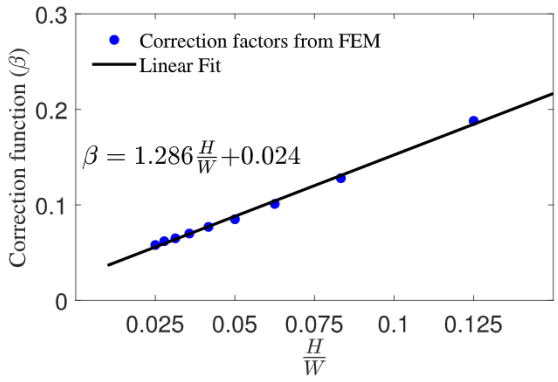

Fig. 4. Variation of ϵ_{13} correction as a function of aspect ratio H/W.

representation for the bending and twisting as the linear C3D8RE elements are known to be stiff under bending. In addition, the solution procedure did not converge for linear elements. An ABAQUS input file that demonstrates combined bending and twisting for P_{45_0} configuration is also provided in the supplementary information.

To calculate the curvatures of the deformed shape obtained from the numerical results, the nodal displacements $\boldsymbol{u}_n$ of the nodes along the length direction are obtained from the top right corner of the bilayer. From the undeformed nodal coordinates $\boldsymbol{X}_n$, the deformed nodal coordinates $\boldsymbol{f}_n$ are calculated as shown in Eq. (37).

$$\boldsymbol{x}_n = \boldsymbol{f}_n = \boldsymbol{u}_n + \boldsymbol{X}_n \tag{37}$$

From differential geometry (Kreyszig, 1968), magnitude of curvatures of the space curve $\boldsymbol{f}(s)$ are obtained using its first, second and third order derivatives $\boldsymbol{f}'(s)$, $\boldsymbol{f}''(s)$, $\boldsymbol{f}'''(s)$ as shown in Eqs. (38a) and (38b), where 's' is the parameter along the length. The derivation for curvatures is given in Appendix B.

$$\kappa = |\mathbf{f}''(s)| \tag{38a}$$

$$\tau = \frac{|(\mathbf{f}'(s) \times \mathbf{f}''(s)).\, \mathbf{f}'''(s)|}{\kappa^2} \tag{38b}$$

To obtain derivatives at a particular node 'n', forward finite difference scheme is used as shown in Eq. (39). Curvatures calculated from different finite difference schemes are found to be quite close. Curvatures calculated from different locations within a cross-section are also found to be quite close.

$$\boldsymbol{f}_n^{(i)} = \frac{\boldsymbol{f}_{n+1}^{(i-1)} - \boldsymbol{f}_n^{(i-1)}}{|\boldsymbol{f}_{n+1} - \boldsymbol{f}_n|} \quad i = 1, 2, 3 \tag{39}$$

5. Results and discussion

To analyze the effect of various geometric parameters and magnitude of the electric field on the deformation of the bilayer, the following parameters shown in Table 2 are used. For the study on a given variable, all other variables are kept constant at these specified values. P_{45_0} configuration is chosen because it exhibits both twisting and bending.

5.1. Variation of curvatures along the length of MFC

Fig. 5 a and b (light color lines) show variation of bending curvature κ and twisting curvature τ calculated from the nodal displacements as mentioned in Section 4 along the length for P_{45_0} configuration. It can be observed from Fig. 5 that both κ and τ are noisy throughout. These noise levels didn't decrease even with a dense mesh. Noise is present in the curvatures data because solution space obtained using quadratic shape functions is differentiable once, while the measurement of κ involves second-order derivatives and measurement of τ involve third-order derivatives Eqs. (38a) and (38b). While noise for κ is small, noise for τ is very high. Since τ has third-order derivatives, errors associated with it are high compared to κ. Therefore, curvature results are locally smoothened using MATLAB. The smoothened data for κ, τ is shown in Fig. 5a and b in dark colors, respectively. The smoothened data is used for further curvature calculation.

From Fig. 5, it can be observed that at a region roughly 10% away from both fixed and free ends, curvatures remain almost constant. Both κ, τ go to high values at boundaries due to fixed and free end constraints. Hence, curvatures for a particular configuration are reported by taking the median of the data in the region away from boundaries $[0.1L\ 0.9L]$. Median is found to be the best metric for smoothened data in τ compared to mean in terms of smoothness with variation in parameters. Mean and median values for κ are found to be quite close and very smooth variation in parameters. Invariance of curvature along the length means that the deformation is a pure helical configuration with constant bending κ and constant twisting τ, thus validating our assumption of deformed shape in strain component calculation in Section 3.2.

5.2. Effect of electric field magnitude on curvatures

Since the electric field is taken to be always oriented along the poling direction in the fibers, the effect of its magnitude is studied. To go into large deformation compared to Rosario (2016), a large electric field (10 MV/m) is applied. For numerical simulations, magnitude of electric field is increased from 0 to 10 MV/m in steps of 0.5 MV/m, while keeping all other parameters in Table 2 the same.

These large electric fields might introduce material nonlinearity arising out of domain switching, mechanical failure due to high stresses, dielectric break down or a culmination of all three. All these effects are ignored and the material is considered to be purely linear piezoelectric.

Fig. 6a and b shows variation of bending curvature κ and twisting curvature τ with electric field. Both κ, τ vary almost linearly with the electric field magnitude. The analytical model also captures this trend very well. Stress-free displacement mismatch scales linearly with the applied electric field since MFC is assumed to be a linear elastic piezoelectric material. As a result, the curvatures scale linearly with the electric field.

5.3. Effect of fiber orientation of MFC on curvatures

Fiber orientation plays an important role in generating anisotropy. To study the effect of fiber orientation on curvatures, two different configurations are studied. First is the family that always produces some bending $\theta_b = 0°$ and second is the family that always produces some twisting $\theta_b = 45°$, unless both layers are identical.

5.3.1. Effect of fiber orientation of MFC on curvatures when bottom layer fiber orientation is fixed at 0 °

Bottom layer fiber orientation θ_b is fixed at 0° and top layer fiber orientation θ_t is varied between 0° to 180°, in steps of 5° for numerical simulations while keeping all the other parameters in Table 2 the same. $\theta_t \in [180° 360°]$ is equivalent to [0° 180°] because of piezoelectric behavior as mentioned in Section 2.

Fig. 7 a shows variation of curvatures with θ_t for $P_{\theta_{t_0}}$ configuration. The resulting deformed shapes are depicted in Fig. 7b. Stress-free displacement mismatch between top and bottom layers for this configuration is given by Eq. (40).

$$\boldsymbol{u}^*_{\theta_{t-0}} = \boldsymbol{u}^*_{\theta_t} - \boldsymbol{u}^*_0 = E_0 d_{33} L \left[(\cos^2(\theta_t) - 1) \quad \frac{1}{2}\sin(2\theta_t) \right]^T \tag{40}$$

From Fig. 7a bending curvature κ and twisting curvature τ are zero when $\theta_t = 0°$, because both layers are identical and stress-free displacement mismatch given by Eq. (40) is zero. From Eq. (40), normal displacement mismatch is maximum and transverse displacement mismatch is zero when $\theta_t = 90°$. On the other hand the transverse displacement mismatch is maximum and normal displacement mismatch is non-zero when $\theta_t = 45°$. Hence κ is maximum and τ is zero when $\theta_t = 90°$ resulting in pure bending as shown in Fig. 7b. On the other hand, τ is maximum and κ is non-zero for when $\theta_t = 45°$ resulting in a helical deformation as shown in Fig. 7b.

The analytical model predicts these FEM trends closely. There is a

Table 2
Parameters for parametric studies.

Parameter	E_0	L	W	H	θ_t	θ_b
Value	$10\ \frac{MV}{m}$	200 mm	10 mm	0.5 mm	45°	0°

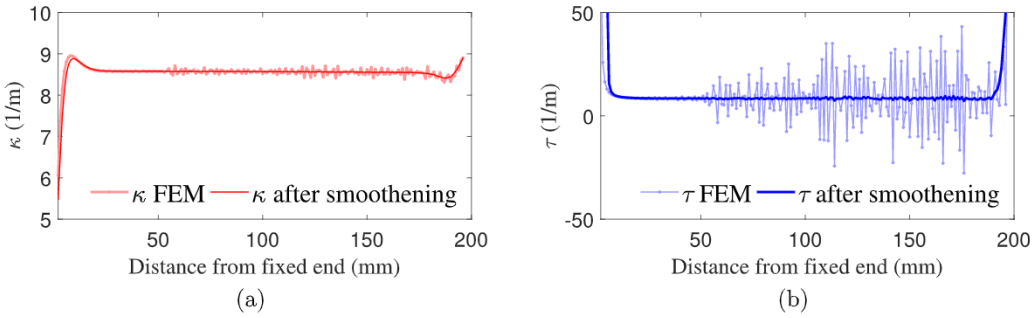

Fig. 5. Variation of (a) bending curvature, κ and (b) twisting curvature τ obtained from FEM simulations (light color line) and from local smoothening (dark color lines) along the length of the bilayer measured from the fixed end. Noise is more for twist curvature because of the third order differentiation involved.

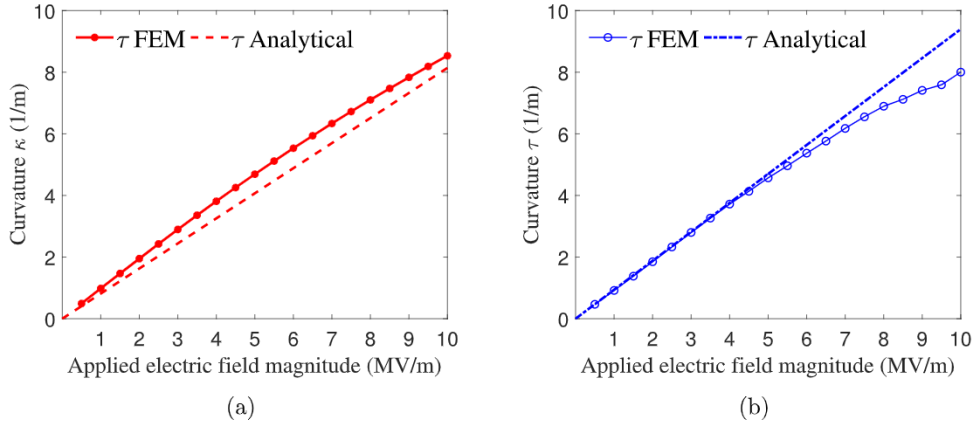

Fig. 6. Variation of (a) bending curvature κ and (b) twisting curvature τ, with electric field for P_{45_0} configuration.

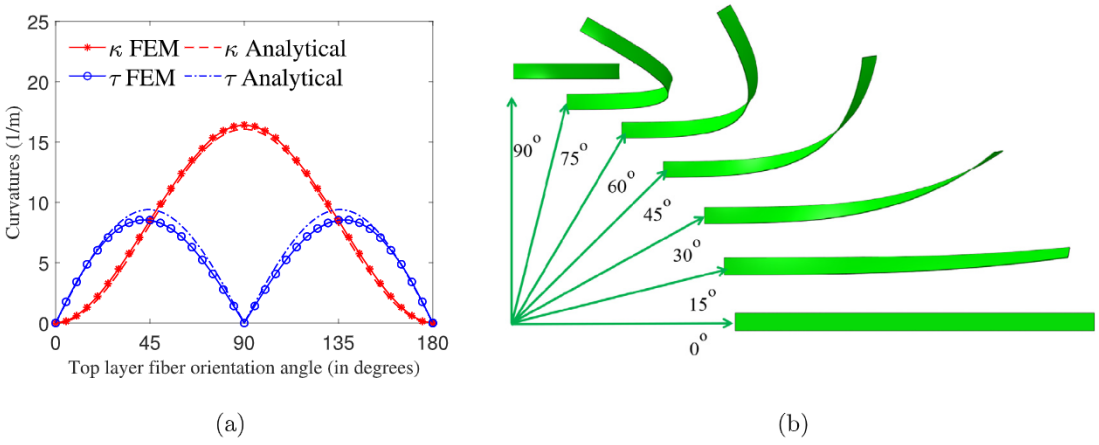

Fig. 7. (a) Variation of bending and twisting curvatures with top layer fiber orientation θ_t for $P_{\theta_t_0}$ configuration. (b) Corresponding top views of finite element deformed shapes.

slight mismatch between FEM and the analytical model for both curvatures. The mismatch between FEM and the analytical model could be attributed to a small mismatch in correction factors since correction function is calculated from fiber orientation resulting in pure twisting and is used for all other fiber orientations. In terms of qualitative trends, the deviation of τ from analytical to FEM is more compared to κ. Since κ is a measure of bending, the effect of warping corrections on κ is quite less and hence very negligible deviation from analytically predicted trends for other fiber orientations. Exact closed-form expressions for curvatures are quite lengthy due to fourth-order elasticity tensor transformations involved and can be obtained from the MATLAB code attached in the supplementary information. The corresponding exact closed-form expression for bending curvature $\kappa_{\theta_t_0}$ for P_{θ_0} configuration is provided in the Appendix D as an indication to show how long the expressions can be. It is hard to get a good idea of physics from the lengthy expressions. A simplified version of curvatures can be obtained as shown in Eqs. (41a) and (41b) for an elastically isotropic material (i.e., $\boldsymbol{C}$ is isotropic).

$$\kappa_{\theta_t_0} \approx \frac{3}{2}\frac{E(e_{33}-e_{31})\sin(\theta_t)^2}{C_{11}H} \tag{41a}$$

$$\tau_{\theta_t_0} \approx \frac{3}{2}\frac{E(e_{33}-e_{31})\sin(2\theta_t)}{(C_{11}-C_{12})\left(2.65H+0.017W+0.057\frac{W^2}{100H}\right)} \tag{41b}$$

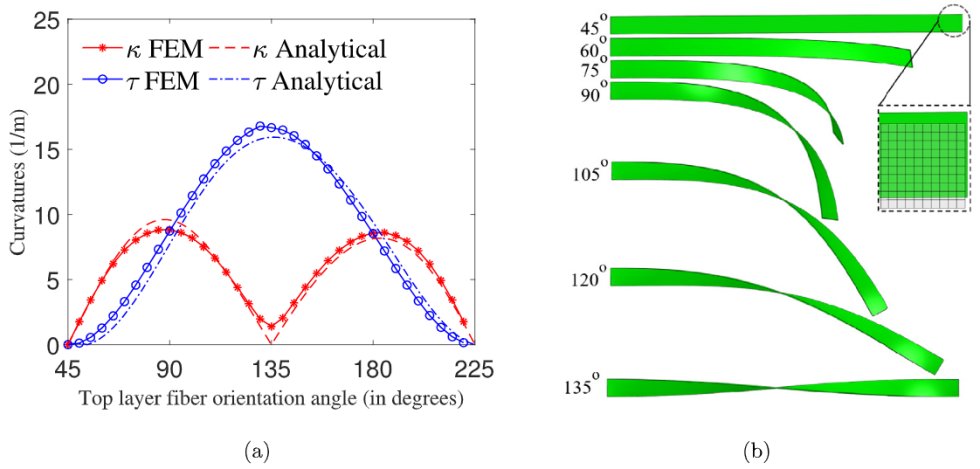

Fig. 8. (a) Variation of bending and twisting curvatures with top layer fiber orientation θ_t for $P_{\theta_t_45}$ configuration. (b) Corresponding top views of finite element deformed shapes.

5.3.2. Effect of fiber orientation on curvatures when bottom layer fiber orientation is fixed at 45 °

Bottom layer fiber orientation θ_b is fixed at 45° and top layer fiber orientation θ_t is varied between 45° to 225°, in steps of 5° for numerical simulations while keeping all the other parameters in Table 2 the same. $\theta_t \in [225^\circ\ 405^\circ]$ is equivalent to [45° 225°] because of piezoelectric behavior as mentioned in Section 2.

Fig. 8 a shows the variation of curvatures with θ_t for $P_{\theta_t_45}$ configurations. The resulting deformed shapes are depicted in Fig. 8b. Stress-free displacement mismatch between top and bottom layers for this particular configuration is given by Eq. (42).

$$\boldsymbol{u}^*_{\theta_t-45} = \boldsymbol{u}^*_{\theta_t} - \boldsymbol{u}^*_{45} = E_0 d_{33} L \left[\left(\cos^2(\theta_t) - \frac{1}{2} \right) \ \frac{1}{2}(\sin(2\theta_t) - 1) \right]^T \tag{42}$$

From Fig. 8a bending curvature κ and twisting curvature τ are zero when $\theta_t = 45°$, because both layers are identical and stress-free displacement mismatch given by Eq. (42) is zero. The inset in Fig. 8b shows the stress-free displacement state of bilayer when $\theta_t = 45°$, i.e., when both layers are oriented at 45°. It can be observed that the bilayer is undergoing in-plane deformation with both normal and transverse displacements in a similar way as depicted in Fig. 2 for general θ.

From Eq. (42), normal displacement mismatch is maximum and transverse displacement mismatch is non-zero when $\theta_t = 90°$ or 180°. On the other hand, transverse displacement mismatch is maximum and normal displacement mismatch is zero when $\theta_t = 135°$. Hence κ is maximum and τ is non-zero when $\theta_t = 90°$ or 180° resulting in a helical deformation as shown in Fig. 8b. On the other hand, τ is maximum and κ is zero when $\theta_t = 135°$ resulting in a pure twisting deformation as shown in Fig. 8b. Animations showing MFC undergoing pure bending for P_{90_0} configuration, pure twisting for P_{45_135} and general helical deformation for P_{45_0} can be found in the supplementary information.

The analytical model predicts these FEM trends closely. Again, the small mismatch between analytical and FEM results could be attributed to the error in correction function as discussed in Section 5.3.1. Again, a simplified version of curvatures can be obtained similar to Eq. (41) in Section 5.3.1 for an elastically isotropic material (i.e., $\boldsymbol{C}$ is isotropic) as shown in Eqs. (43a) and (43b).

$$\kappa_{\theta_45} \approx \frac{3}{4} \frac{E(e_{31} - e_{33})\cos(2\theta_t)}{C_{11} H} \tag{43a}$$

$$\tau_{\theta_45} \approx \frac{3}{2} \frac{E(e_{33} - e_{31})(\sin(2\theta_t) - 1)}{(C_{11} - C_{12})\left(2.65H + 0.017W + 0.057\frac{W^2}{100H}\right)} \tag{43b}$$

5.4. Effect of length (L) of MFC on curvatures

The length of the bilayer is varied from 100 mm to 300 mm, in steps of 20 mm for numerical analysis, while keeping all other parameters in Table 2 the same. Fig. 9a shows variation of curvatures with length for general twisting P_{45_0} configuration. It can be observed that curvatures (κ, τ) do not depend on the length of MFC. The analytical model also captures this length independence very well as shown in Eqs. (41a) and (41b). The length independence is observed not only for P_{45_0} configuration but for all $P_{\theta_t_\theta_b}$ configurations. The length independence is also a well-known phenomenon in other bending based shape morphing structures. The above phenomenon is because of the uniform mismatch

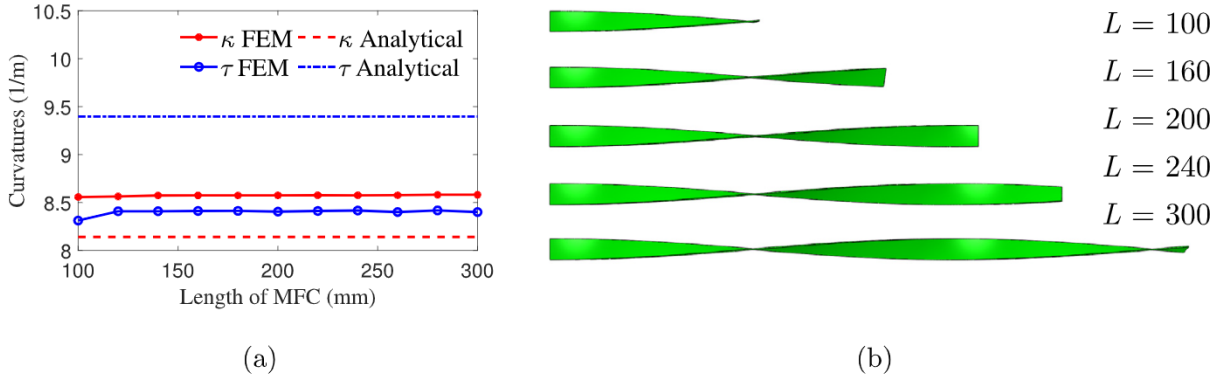

Fig. 9. (a) Variation of bending and twisting curvatures with length for PP_{45_0} configuration. (b) The bilayer deformations showing the length independence in pure twisting for PP_{45_-45} configuration.

in strain generated throughout the bilayer. From Fig. 9a there is an error of about 5% in κ estimation and 10% in τ estimation between analytical and FEM results. Again, the mismatch between analytical and FEM results could be attributed to the error in correction function as discussed in Section 5.3.1.

The independence of curvatures on the length is clearly understood from Fig. 9b which depicts deformed shapes for pure twisting P_{45_-45} configuration for different lengths at the same electric field. It can be seen that the amount of tip rotation scales linearly with length but rotation per unit length, which is equivalent to τ, remains almost the same. Based on this length independence, one can think of the following non-dimensional numbers given by Eqs. (44a) and (44b) that would provide an estimation of deformation. When $(\kappa^*, \tau^*) = (\pi, 0)$, it is indicative of bilayer deforming into a semi-circular arc. On the other hand, when $(\kappa^*, \tau^*) = (0,\pi)$, it is indicative of the bilayer twisting by 180° at the free end and a compound effect when both curvatures are non-zero.

$$\kappa^* = L\kappa \tag{44a}$$

$$\tau^* = L\tau \tag{44b}$$

For example, from Fig. 8a for pure twisting configuration (P_{45_-45}), $L = 0.2$ m, $\tau_{max} \approx 17$ and $\tau^*_{max} = 0.2 \times 17 = 3.4 \approx \pi$, resulting in rotation of approximately 180° at free end which can be clearly observed in Fig. 8b.

5.5. Effect of width (W) of MFC on curvatures

The width of the MFC is varied from 4 mm to 20 mm, in steps of 2 mm for numerical analysis, while keeping all other variables in Table 2 the same. Fig. 10a shows variation of curvatures with width for P_{45_0} configuration. Both bending curvature κ and twisting curvature τ decrease with an increase in width. The analytical model predicts independence of κ with width and fails to capture the decreasing trend. From Fig. 10b, it can be observed that κ for pure bending configuration (P_{90_0}) decreases with an increase in width W but approaches a constant value at higher widths and the analytical model captures just this independence of κ on W. Decrease of κ with W might be due to MFC transitioning away from plane stress scenario and in the analytical model these boundary effects are not considered. On the other hand, from Fig. 10a it can be observed that twisting curvature τ decreases nonlinearly with an increase in width W and the nonlinear variation might be due to warping. Analytical model closely captures these trends on τ at higher aspect ratio W/H and deviates at lower aspect ratio W/H, probably because of error in approximating strain.

5.6. Effect of thickness(H) of MFC on curvatures

The total thickness H of the MFC is varied from 0.2 mm to 1 mm, in steps of 0.1 mm for numerical analysis, while keeping all other parameters in Table 2 the same. Fig. 11a and b shows variation of curvatures with thickness for P_{45_0} configuration. Both twisting and bending curvatures decrease with an increase in thickness. The analytical model captures these trends closely. From Eq. (41a) curvature κ show a rough variation with H as H^{-1}. This is a well-known result even in other bending based shape morphing structures. On the other hand, twisting curvature τ shows a nonlinear variation with H due to warping in Eq. (41b) but is predominantly a H^{-1} variation as thickness increases.

6. Conclusion

An analytical model to predict the evolution of curvatures as a function of system parameters (length, width, thickness, fiber orientation and electric field magnitude) for the combined bending and twisting based shape-morphing in anisotropic piezo macro fiber composites is developed. An energy minimization approach is adopted to derive the analytical expressions. A comprehensive physical explanation for twisting is provided based on stress-free strain mismatch. The material anisotropy plays a crucial role in governing twisting. The energy minimization based approach presented in this paper would guide designers not only in piezo-based twisting systems but in any other stimuli-responsive systems involving combined bending and twisting. The effects of warping are incorporated through a correction function. However, a detailed analytical model incorporating the effects of warping forms the scope of future studies. Although, the results discussed in this paper suggest the application of large electric fields that are not usually feasible, we hope that this work provides guidelines for future shape-morphing structures made of new age low-stiffness smart materials like liquid crystal elastomers, magnetic particle embedded hydrogels with experimentally realizable intensity of the stimulus.

Declaration of Competing Interests

The authors declare that they have no known competing financial interests or personal relationships that could have appeared to influence the work reported in this paper.

CRediT authorship contribution statement

Jagannadh Boddapati: Conceptualization, Methodology, Formal analysis, Investigation, Validation, Writing - original draft. **Shaswat Mohanty:** Conceptualization, Formal analysis, Validation, Writing -

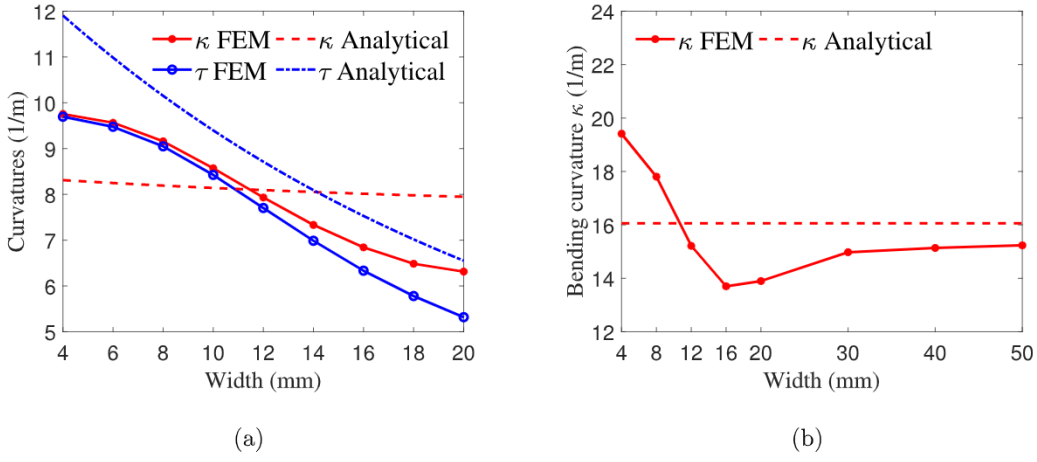

Fig. 10. (a) Variation of bending and twisting curvatures with width for P_{45_0} configuration. (b) Variation of bending curvature with width for pure bending case with P_{90_0} configuration. Curvature κ approaches a constant value at large widths and the analytical model captures only this width independence.

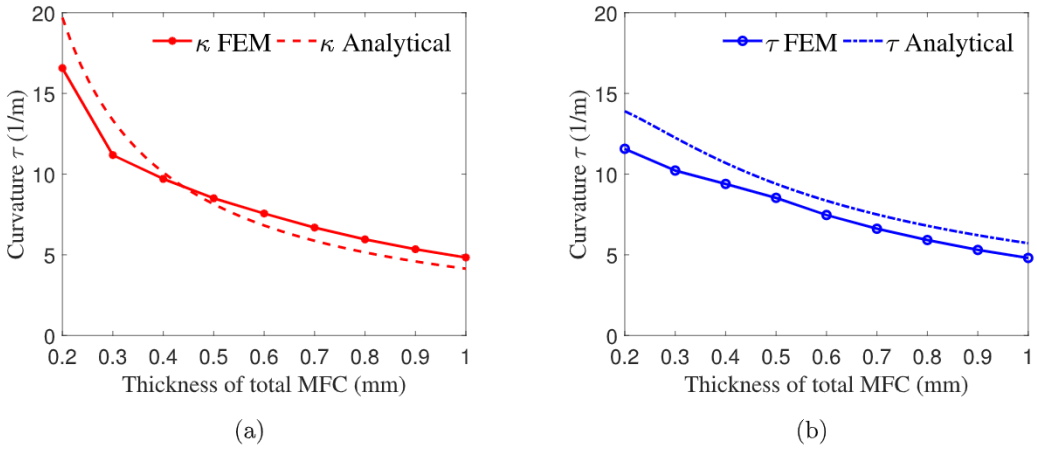

Fig. 11. (a) Variation of bending and curvature with thickness of MFC showing 1/H variation. (b) Variation of twisting curvature with thickness of MFC also captures the thickness dependence of τ.

original draft. **Ratna Kumar Annabattula:** Conceptualization, Resources, Supervision, Writing - review & editing.

Acknowledgment

We thank Prof. Kaushik Bhattacharya for his valuable insights during the discussions on the analytical model development.

Appendix A. Transformed tensor components

Components of the second order dielectric permittivity tensor after transformation are shown in Eq. (A.1). Components of the third order piezoelectric strain tensor after transformation are shown in Eq. (A.2). Components of the fourth order elastic stiffness tensor after transformation are shown in Eq. (A.3), and Table A.3.

$$\boldsymbol{K}' = \begin{bmatrix} K_{11}\sin^2\theta + K_{33}\cos^2\theta & \frac{1}{2}(K_{33} - K_{11})\sin 2\theta & 0 \\ \frac{1}{2}(K_{33} - K_{11})\sin 2\theta & K_{11}\cos^2\theta + K_{33}\sin^2\theta & 0 \\ 0 & 0 & K_{11} \end{bmatrix} \tag{A.1}$$

Table A.3
Components of transformed stiffness matrix.

Global	Relation in terms of local coordinate components
C'_{11}	$C_{33}\cos(\theta)^4 - \frac{1}{4}(2C_{44} + C_{13})(\cos(4\theta) - 1) + C_{11}\sin(\theta)^4$
C'_{22}	$C_{11}\cos(\theta)^4 - \frac{1}{4}(2C_{44} + C_{13})(\cos(4\theta) - 1) + C_{33}\sin(\theta)^4$
C'_{33}	C_{11}
C'_{44}	$\frac{1}{2}(C_{11} - C_{12})\sin(\theta)^2 + C_{44}\cos(\theta)^2$
C'_{55}	$\frac{1}{2}(C_{11} - C_{12})\cos(\theta)^2 + C_{44}\sin(\theta)^2$
C'_{66}	$\frac{1}{8}(C_{11} - 2C_{13} + C_{33} + 4C_{44}) - \frac{1}{8}\cos(4\theta)(C_{11} - 2C_{13} + C_{33} - 4C_{44})$
$C'_{12} = C'_{21}$	$\frac{1}{8}(C_{11} + 6C_{13} + C_{33} - 4C_{44}) - \frac{1}{8}\cos(4\theta)(C_{11} - 2C_{13} + C_{33} - 4C_{44})$
$C'_{13} = C'_{31}$	$C_{13} - C_{13}\sin(\theta)^2 + C_{12}\sin(\theta)^2$
$C'_{16} = C'_{61}$	$\frac{1}{8}\sin(4\theta)(C_{11} - 2C_{13} + C_{33} - 4C_{44}) + \frac{1}{4}\sin(2\theta)(C_{33} - C_{11})$
$C'_{23} = C'_{32}$	$C_{12}(1 - \sin(\theta)^2) + C_{13}\sin(\theta)^2$
$C'_{26} = C'_{62}$	$-\frac{1}{8}\sin(4\theta)(C_{11} - 2C_{13} + C_{33} - 4C_{44}) + \frac{1}{4}\sin(2\theta)(C_{33} - C_{11})$
$C'_{36} = C'_{63}$	$-\frac{1}{2}\sin(2\theta)(C_{12} - C_{13})$
$C'_{45} = C'_{45}$	$\frac{1}{4}\sin(2\theta)(C_{12} - C_{11} + 2C_{44})$

$$\boldsymbol{e}' = \begin{bmatrix} e_{33}\cos^3\theta + e_{31}\cos\theta\sin^2\theta + e_{15}\sin\theta\sin2\theta & e_{31}\sin^3\theta + e_{33}\cos^2\theta\sin\theta - e_{15}\cos\theta\sin2\theta & 0 \\ e_{31}\cos^3\theta + e_{33}\cos\theta\sin^2\theta - e_{15}\sin\theta\sin2\theta & e_{33}\sin^3\theta + e_{31}\cos^2\theta\sin\theta + e_{15}\cos\theta\sin2\theta & 0 \\ e_{31}\cos\theta & e_{31}\sin\theta & 0 \\ 0 & 0 & e_{15}\sin\theta \\ 0 & 0 & e_{15}\cos\theta \\ (e_{33} - e_{31})\cos^2\theta\sin\theta - e_{15}\sin\theta\cos2\theta & (e_{33} - e_{31})\cos\theta\sin^2\theta + e_{15}\cos\theta\cos2\theta & 0 \end{bmatrix} \tag{A.2}$$

$$\boldsymbol{C}' = \begin{bmatrix} C'_{11} & C'_{12} & C'_{13} & 0 & 0 & C'_{16} \\ C'_{12} & C'_{22} & C'_{13} & 0 & 0 & C'_{26} \\ C'_{13} & C'_{23} & C'_{33} & 0 & 0 & C'_{36} \\ 0 & 0 & 0 & C'_{44} & C'_{45} & 0 \\ 0 & 0 & 0 & C'_{54} & C'_{55} & 0 \\ C'_{16} & C'_{26} & C'_{36} & 0 & 0 & C'_{66} \end{bmatrix} \tag{A.3}$$

Appendix B. Curvature calculation using space curve derivatives

The parametrized coordinates of a helical space curve are given by Eq. (B.1). The spatial derivatives of the parametrized coordinates are given by Eqs. (B.2) and (B.4)

$$\boldsymbol{f}(s) = \frac{\kappa}{\gamma^2}\sin(\gamma s)\mathbf{e}_1 + \frac{\kappa}{\gamma^2}(\cos(\gamma s) - 1)\mathbf{e}_2 + \frac{\tau}{\gamma}s\mathbf{e}_3 \tag{B.1}$$

$$\frac{\mathrm{d}\boldsymbol{f}}{\mathrm{d}s} = \boldsymbol{f}'(s) = \frac{\kappa}{\gamma}\cos(\gamma s)\mathbf{e}_1 - \frac{\kappa}{\gamma}\sin(\gamma s)\mathbf{e}_2 + \frac{\tau}{\gamma}\mathbf{e}_3 \tag{B.2}$$

$$\frac{\mathrm{d}\boldsymbol{f}'}{\mathrm{d}s} = \boldsymbol{f}''(s) = -\kappa\,\sin(\gamma s)\mathbf{e}_1 - \kappa\cos(\gamma s)\mathbf{e}_2 \tag{B.3}$$

$$\frac{\mathrm{d}\boldsymbol{f}''}{\mathrm{d}s} = \boldsymbol{f}'''(s) = -\kappa\gamma\,\cos(\gamma s)\mathbf{e}_1 + \kappa\gamma\sin(\gamma s)\mathbf{e}_2 \tag{B.4}$$

Upon calculating the following vector products in Eqs. (B.5) and (B.6), curvatures κ, τ are obtained as shown in Eqs. (B.7) and (B.8), where box indicates scalar vector triple product.

$$\boldsymbol{f}'(s) \times \boldsymbol{f}''(s) = \frac{\tau\kappa}{\gamma}\cos(\gamma s)\mathbf{e}_1 - \frac{\tau\kappa}{\gamma}\sin(\gamma s)\mathbf{e}_2 - \frac{\kappa^2}{\gamma}\mathbf{e}_3 \tag{B.5}$$

$$(\boldsymbol{f}'(s) \times \boldsymbol{f}''(s)).\,\boldsymbol{f}'''(s) = -\tau\kappa^2 \tag{B.6}$$

$$\kappa = |\boldsymbol{f}''(s)| \tag{B.7}$$

$$\tau = \frac{|[\boldsymbol{f}'(s), \boldsymbol{f}''(s), \boldsymbol{f}'''(s)]|}{\kappa^2} \tag{B.8}$$

For pure twisting structure, $\kappa = 0$, $\tau \neq 0$. Therefore it is hard to evaluate τ from nodal coordinates of the centerline in that case using the above formula Eq. (B.8). However, this problem is resolved if κ is evaluated at a location not along the central line which results in non-zero κ (but small as shown in Fig. 8a) even for pure twisting case. Therefore, for uniformity among different cases, curvatures are always evaluated from the nodes at top right corner of the MFC.

Appendix C. Mesh refinement analysis

Mesh refinement analysis is performed by taking tip displacement magnitude (δ_e) as a performance parameter. Since the thickness of the bilayer is an order of magnitude smaller than the length and the width, the study focused on number of elements through the thickness. While studying mesh refinement along the length and the width directions, the study focused on the element size. The results are summarized in the tables Tables C.4–C.6.

Along thickness

A convergence in the δ_e values is observed at around 3–4 elements through the thickness of a single layer as seen in Table C.4. For this analysis, mesh size along the length and the width directions is fixed at 1 mm. To reduce computational time, the remainder of the study has been carried out with 3 elements along the thickness of each MFC layer.

Along length

A convergence in the δ_e values is observed for an element length of 1 mm and lesser as seen in Table C.5. For this analysis, mesh size along the

Table C.4
Mesh refinement analysis for element size along the thickness of the bilayer.

Number of elements in each layer	1	2	3	4	5
δ_e (mm)	74.4	77.3	79.9	79.9	80.0

Table C.5
Mesh refinement analysis for element size along the length of the bilayer.

Element length (mm)	5	3	2	1	$\frac{2}{3}$	$\frac{1}{2}$
δ_e (mm)	64.6	72.6	75.5	79.7	80.0	80.0

Table C.6
Mesh refinement analysis for element size along the width of the bilayer.

Element length (mm)	5	3	2	1	$\frac{2}{3}$	$\frac{1}{2}$
δ_e (mm)	71.2	75.8	77.9	79.7	79.9	80.0

width direction is fixed at 1 mm while number of elements through the thickness is fixed at 3 elements for each MFC layer. To reduce computational time, the remainder of the study has been carried out with an element size of 1 mm along the length of the bilayer.

Along width

A convergence in the δ_e values is observed for an element length of 1 mm and lesser as seen in Table C.6. For this analysis, mesh size along the length direction is fixed at 1 mm while number of elements through the thickness is fixed at 3 elements for each MFC layer. To reduce computational time, the remainder of the study has been carried out with an element size of 1mm along the width of the bilayer.

Appendix D. Exact curvature expression

Eq. (D.1) shows the exact analytical form of the bending curvature κ_{θ_0} when the fiber orientation angle in the bottom layer is 0°. The transformation of the coordinate systems results in an expanisve numerator and denominator, which have been denoted by $N1_{\theta_0}$ and $D1_{\theta_0}$, respectively. Eqs. (D.2) and (D.3) gives the exact form of $N1_{\theta_0}$ and $D1_{\theta_0}$.

$$\kappa_{\theta_0} = \frac{24E(e_{31}-e_{33})(\cos(2\theta)-1)}{H}\frac{N1_{\theta_0}}{D1_{\theta_0}} \tag{D.1}$$

$$\begin{aligned} N1_{\theta_0} = {} & 2C_{33}H^2 - 2C_{13}H^2 + 4C_{44}H^2 - 2C_{13}H^2\cos(2\theta) + 2C_{33}H^2\cos(2\theta) - \\ & 4C_{44}H^2\cos(2\theta) + C_{11}\beta^2W^2 - C_{12}\beta^2W^2 + 6C_{44}\beta^2W^2 - C_{11}\beta^2W^2\cos(2\theta) + \\ & C_{12}\beta^2W^2\cos(2\theta) + 2C_{44}\beta^2W^2\cos(2\theta) \end{aligned} \tag{D.2}$$

$$\begin{aligned} D1_{\theta_0} = {} & 8C_{33}^2H^2 - 8C_{13}^2H^2 + 32C_{44}^2H^2 + 10C_{11}^2\beta^2W^2 + 48C_{44}^2\beta^2W^2 + \\ & 16C_{11}C_{33}H^2 - 16C_{13}C_{33}H^2 + 48C_{11}C_{44}H^2 + 144C_{33}C_{44}H^2 + 8C_{13}^2H^2\cos(4\theta) - \\ & 8C_{33}^2H^2\cos(4\theta) - 32C_{44}^2H^2\cos(4\theta) - 10C_{11}C_{12}\beta^2W^2 + 4C_{11}C_{13}\beta^2W^2 - \\ & 4C_{12}C_{13}\beta^2W^2 + 18C_{11}C_{33}\beta^2W^2 - 18C_{12}C_{33}\beta^2W^2 + 36C_{11}C_{44}\beta^2W^2 - \\ & 8C_{12}C_{44}\beta^2W^2 + 24C_{13}C_{44}\beta^2W^2 + 140C_{33}C_{44}\beta^2W^2 - 15C_{11}^2\beta^2W^2\cos(2\theta) + \\ & 6C_{11}^2\beta^2W^2\cos(4\theta) - C_{11}^2\beta^2W^2\cos(6\theta) + 8C_{44}^2\beta^2W^2\cos(2\theta) - \\ & 48C_{44}^2\beta^2W^2\cos(4\theta) - 8C_{44}^2\beta^2W^2\cos(6\theta) - 16C_{11}C_{33}H^2\cos(4\theta) + \\ & 16C_{13}C_{33}H^2\cos(4\theta) - 64C_{11}C_{44}H^2\cos(2\theta) + 16C_{11}C_{44}H^2\cos(4\theta) + \\ & 64C_{33}C_{44}H^2\cos(2\theta) + 48C_{33}C_{44}H^2\cos(4\theta) + 15C_{11}C_{12}\beta^2W^2\cos(2\theta) - \\ & 2C_{11}C_{13}\beta^2W^2\cos(2\theta) - 6C_{11}C_{12}\beta^2W^2\cos(4\theta) + 2C_{12}C_{13}\beta^2W^2\cos(2\theta) - \\ & 4C_{11}C_{13}\beta^2W^2\cos(4\theta) + C_{11}C_{12}\beta^2W^2\cos(6\theta) + 4C_{12}C_{13}\beta^2W^2\cos(4\theta) + \\ & 2C_{11}C_{13}\beta^2W^2\cos(6\theta) - 2C_{12}C_{13}\beta^2W^2\cos(6\theta) - 15C_{11}C_{33}\beta^2W^2\cos(2\theta) + \\ & 15C_{12}C_{33}\beta^2W^2\cos(2\theta) - 2C_{11}C_{33}\beta^2W^2\cos(4\theta) + 2C_{12}C_{33}\beta^2W^2\cos(4\theta) - \\ & C_{11}C_{33}\beta^2W^2\cos(6\theta) + C_{12}C_{33}\beta^2W^2\cos(6\theta) - 38C_{11}C_{44}\beta^2W^2\cos(2\theta) + \\ & 4C_{12}C_{44}\beta^2W^2\cos(2\theta) - 4C_{11}C_{44}\beta^2W^2\cos(4\theta) + 4C_{13}C_{44}\beta^2W^2\cos(2\theta) + \\ & 8C_{12}C_{44}\beta^2W^2\cos(4\theta) + 6C_{11}C_{44}\beta^2W^2\cos(6\theta) - 24C_{13}C_{44}\beta^2W^2\cos(4\theta) - \\ & 4C_{12}C_{44}\beta^2W^2\cos(6\theta) - 4C_{13}C_{44}\beta^2W^2\cos(6\theta) + 94C_{13}C_{44}\beta^2W^2\cos(6\theta) + \\ & 20C_{33}C_{44}\beta^2W^2\cos(4\theta) + 2C_{33}C_{44}\beta^2W^2\cos(6\theta) \end{aligned} \tag{D.3}$$

Supplementary material

Supplementary material associated with this article can be found, in the online version, at 10.1016/j.mechmat.2020.103350

References

Abdullah, A.M., Li, X., Braun, P.V., Rogers, J.A., Hsia, K.J., 2018. Self-folded gripper-like architectures from stimuli-responsive bilayers. Adv. Mater. 30 (31), 1801669.

Alcock, S.G., Nistea, I., Sutter, J.P., Sawhney, K., Fermé, J.-J., Thellièr, C., Peverini, L., 2015. Characterization of a next-generation piezo bimorph X-ray mirror for synchrotron beamlines. J. Synchrotron Radiat. 22 (1), 10–15.

Armon, S., Efrati, E., Kupferman, R., Sharon, E., 2011. Geometry and mechanics in the opening of chiral seed pods. Science 333 (6050), 1726–1730.

Bent, A.A., Hagood, N.W., 1997. Piezoelectric fiber composites with interdigitated electrodes. J. Intell. Mater. Syst. Struct. 8 (11), 903–919.

Boley, J.W., van Rees, W.M., Lissandrello, C., Horenstein, M.N., Truby, R.L., Kotikian, A., Lewis, J.A., Mahadevan, L., 2019. Shape-shifting structured lattices via multimaterial

4D printing. Proc. Natl. Acad. Sci. 116 (42), 20856–20862.
Cha, J., Daraio, C., 2018. Electrical tuning of elastic wave propagation in nanomechanical lattices at MHz frequencies. Nat. Nanotechnol. 13 (11), 1016.
Chen, P., Peng, J., Liu, H., Gao, F., Guo, W., 2018. The electromechanical behavior of a piezoelectric actuator bonded to a graded substrate including an adhesive layer. Mech. Mater. 123, 77–87.
Chen, Z., Majidi, C., Srolovitz, D.J., Haataja, M., 2011. Tunable helical ribbons. Appl. Phys. Lett. 98 (1), 11906.
Fang, D., Liu, J., 2013. Fracture Mechanics of Piezoelectric and Ferroelectric Solids. Springer.
Gladman, A.S., Matsumoto, E.A., Nuzzo, R.G., Mahadevan, L., Lewis, J.A., 2016. Biomimetic 4D printing. Nat. Mater. 15 (4), 413.
Hasanzadeh, M., Ansari, R., Hassanzadeh-Aghdam, M., 2019. Evaluation of effective properties of piezoelectric hybrid composites containing carbon nanotubes. Mech. Mater. 129, 63–79.
Huang, H.-W., Sakar, M.S., Petruska, A.J., Pané, S., Nelson, B.J., 2016. Soft micromachines with programmable motility and morphology. Nat. Commun. 7, 12263.
Huang, J., Liu, J., Kroll, B., Bertoldi, K., Clarke, D.R., 2012. Spontaneous and deterministic three-dimensional curling of pre-strained elastomeric bi-strips. Soft Matter 8, 6291–6300.
Jeon, S.-J., Hauser, A.W., Hayward, R.C., 2017. Shape-morphing materials from stimuli-responsive hydrogel hybrids. Acc. Chem. Res. 50 (2), 161–169.
Jeong, K.-U., Jang, J.-H., Kim, D.-Y., Nah, C., Lee, J.H., Lee, M.-H., Sun, H.-J., Wang, C.-L., Cheng, S.Z.D., Thomas, E.L., 2011. Three-dimensional actuators transformed from the programmed two-dimensional structures via bending, twisting and folding mechanisms. J. Mater. Chem. 21, 6824–6830.
Kim, Y., Yuk, H., Zhao, R., Chester, S.A., Zhao, X., 2018. Printing ferromagnetic domains for untethered fast-transforming soft materials. Nature 558 (7709), 274.
Kong, X.Y., Wang, Z.L., 2003. Spontaneous polarization-induced nanohelixes, nanosprings, and nanorings of piezoelectric nanobelts. Nano Lett. 3 (12), 1625–1631.
Kotikian, A., McMahan, C., Davidson, E.C., Muhammad, J.M., Weeks, R.D., Daraio, C., Lewis, J.A., 2019. Untethered soft robotic matter with passive control of shape morphing and propulsion. Science Robotics 4 (33), 1–10. Art–No
Kreyszig, E., 1968. Introduction to Differential Geometry and Riemannian Geometry. University of Toronto Press.
Kuang, X., Roach, D.J., Wu, J., Hamel, C.M., Ding, Z., Wang, T., Dunn, M.L., Qi, H.J., 2019. Advances in 4d printing: materials and applications. Adv. Funct. Mater. 29 (2), 1805290.
Lachenal, X., Daynes, S., Weaver, P.M., 2013. Review of morphing concepts and materials for wind turbine blade applications. Wind Energy 16 (2), 283–307.
Lines, M.E., Glass, A.M., 2001. Principles and applications of ferroelectrics and related materials. Oxford University Press.
Liu, J., Huang, J., Su, T., Bertoldi, K., Clarke, D.R., 2014. Structural transition from helices to hemihelices. PLoS One 9, 1–7.
Majidi, C., Chen, Z., Srolovitz, D., Haataja, M., 2010. Spontaneous bending of piezoelectric nanoribbons: mechanics, polarization, and space charge coupling. J. Mech. Phys. Solids 58 (2), 73–85.
Mao, Y., Ding, Z., Yuan, C., Ai, S., Isakov, M., Wu, J., Wang, T., Dunn, M.L., Qi, H.J., 2016. 3D printed reversible shape changing components with stimuli responsive materials. Sci. Rep. 6, 24761.
Martin, N., Gharib, M., 2018. On the role of tip curvature on flapping plates. Bioinspiration Biomim. 13 (2), 026001.
Masoud, H., Bingham, B.I., Alexeev, A., 2012. Designing maneuverable micro-swimmers actuated by responsive gel. Soft Matter 8, 8944–8951.
MFC, 2019. Macro fiber composite. https://www.smart-material.com/media/Datasheets/MFC_V2.3-Web-full-brochure.pdf. Accessed: 2019-09-28.
Nasser, H., Deraemaeker, A., Belouettar, S., 2008. Electric field distribution in macro fiber composite using interdigitated electrodes. Multi-Functional Materials and Structures. Trans Tech Publications Ltd, pp. 1173–1176.
Nikolov, S.V., Yeh, P.D., Alexeev, A., 2014. Self-propelled microswimmer actuated by stimuli-sensitive bilayered hydrogel. ACS Macro Lett. 4 (1), 84–88.
Oliver, K., Seddon, A., Trask, R.S., 2016. Morphing in nature and beyond: a review of natural and synthetic shape-changing materials and mechanisms. J. Mater. Sci. 51 (24), 10663–10689.
Oudich, A., Thiebaud, F., 2016. A two-way shape memory alloy-piezoelectric bimorph for thermal energy harvesting. Mech. Mater. 102, 1–6.
Paradies, R., Ciresa, P., 2009. Active wing design with integrated flight control using piezoelectric macro fiber composites. Smart Mater. Struct. 18 (3), 35010.
Park, J.-S., Kim, J.-H., 2005. Analytical development of single crystal macro fiber composite actuators for active twist rotor blades. Smart Mater. Struct. 14 (4), 745–753.
Randall, C.L., Gultepe, E., Gracias, D.H., 2012. Self-folding devices and materials for biomedical applications. Trends Biotechnol. 30 (3), 138–146.
Rosario, C.M., 2016. On the active deformations of hybrid specimens. Aircr. Eng. Aerosp. Technol. 88 (5), 676–687.
Sadd, M.H., 2014. Chapter 11 - anisotropic elasticity. In: Sadd, M.H. (Ed.), Elasticity, third ed. Academic Press, Boston, pp. 323–368.
Sadd, M.H., 2014. Chapter 9 - extension, torsion, and flexure of elastic cylinders. In: Sadd, M.H. (Ed.), Elasticity, third ed. Academic Press, Boston, pp. 235–279.
Signorato, R., Hignette, O., Goulon, J., 1998. Multi-segmented piezoelectric mirrors as active/adaptive optics components. J. Synchrotron Radiat. 5 (3), 797–800.
Simulia, D. S., 2012. Abaqus 6.12 documentation. Providence, Rhode Island, US 261.
Sofla, A., Meguid, S., Tan, K., Yeo, W., 2010. Shape morphing of aircraft wing: status and challenges. Mater. Des. 31 (3), 1284–1292.
Spillmann, C.M., Naciri, J., Ratna, B.R., Selinger, R.L.B., Selinger, J.V., 2016. Electrically induced twist in smectic liquid crystalline elastomers. J. Phys. Chem. B 120 (26), 6368–6372.
Susini, J., Labergerie, D., Zhang, L., 1995. Compact active/adaptive xray mirror: bimorph piezoelectric flexible mirror. Rev. Sci. Instrum. 66 (2), 2229–2231.
Vyas, N., Annabattula, R. K., 2018. A finite element analysis of rolling of bilayer films to cylindrical and conical tubes. arXiv:1801.04166.
White, T.J., Broer, D.J., 2015. Programmable and adaptive mechanics with liquid crystal polymer networks and elastomers. Nat. Mater. 14 (11), 1087.
Wie, J.J., Lee, K.M., Ware, T.H., White, T.J., 2015. Twists and turns in glassy, liquid crystalline polymer networks. Macromolecules 48 (4), 1087–1092.
Williams, R.B., Park, G., Inman, D.J., Wilkie, W.K., 2002. An overview of composite actuators with piezoceramic fibers. Proceeding of IMAC XX. 47.
Wu, Z.L., Moshe, M., Greener, J., Therien-Aubin, H., Nie, Z., Sharon, E., Kumacheva, E., 2013. Three-dimensional shape transformations of hydrogel sheets induced by small-scale modulation of internal stresses. Nat. Commun. 4, 1586.
Yu, X., Zhang, L., Hu, N., Grover, H., Huang, S., Wang, D., Chen, Z., 2017. Shape formation of helical ribbons induced by material anisotropy. Appl. Phys. Lett. 110 (9), 91901.
Zhang, Q., Zhang, K., Hu, G., 2016. Smart three-dimensional lightweight structure triggered from a thin composite sheet via 3D printing technique. Sci. Rep. 6, 22431.
Zhao, Y., Ikeda, T., 2009. Smart Light-Responsive Materials: Azobenzene-Containing Polymers and Liquid Crystals. John Wiley & Sons.